Hindawi
Shock and Vibration
Volume 2019, Article ID 2593973, 16 pages
https://doi.org/10.1155/2019/2593973

Research Article

A Morphological Filtering Method Based on Particle Swarm Optimization for Railway Vehicle Bearing Fault Diagnosis

Yan Huang, Jianhui Lin, Zechao Liu, and Chenguang Huang

State Key Laboratory of Traction Power, Southwest Jiaotong University, Chengdu 610031, China

Correspondence should be addressed to Zechao Liu; cap_lzc@my.swjtu.edu.cn

Received 23 July 2019; Revised 2 December 2019; Accepted 3 December 2019; Published 24 December 2019

Academic Editor: Zhixiong Li

With the rapid development of high-speed railway, the fault diagnosis of railway vehicles has become more and more important for ensuring the operating safety. The MF is a nonlinear signal processing method which can extract the modulated faulty information via reshaping the analyzed signal. However, the choices of operators and structure elements (SE) are numerous and complicated to determine the best MF solution for different bearing faulty signals. In this paper, the particle swarm optimization (PSO) was introduced to optimize the effect of MF among several classical MF operators and different SE parameters. The proposed method applied PSO to select the best MF result with respect to the fitness function adopting kurtosis. A set of bearing signals with additional interference of wheel-track excitement are analyzed to verify the effectiveness of the proposed method. The results demonstrated that the proposed method is capable of obtaining the optimized solution and accurately extracting the fault information. Furthermore, the shaft rotation frequency and wheel-track interference were reduced by the proposed method.

1. Introduction

In recent years, with the rapid development of high-speed railway all over the world, the occurrence of various kinds of railway accidents continuously increases [1]. The failure of railway vehicle often causes tremendous casualties and economic losses. Therefore, the safety of the railway vehicle has gained more and more attention from the government, the industry, and the academia. The axle box bearing, which supports the weight of the vehicle and suffers various loads from the wheel set or other components of the bogie, is one of the key rolling components to guarantee the safety operation of the railway vehicle [2]. Therefore, the fault diagnosis of axle box bearing is crucial for the operation safety of the railway vehicle [3]. Vibration signal is commonly applied for rotational machinery fault diagnosis because of its convenience and efficiency. However, the vibrational measurement of the axle box bearing suffers strong interference from other components in the railway vehicle system, such as rail track irregularity and wheel defect [4]. Moreover, this interference, especially wheel-rail excitement, is normally dominant in an axle box bearing vibration signal, which increases the difficulty of the diagnosis [5]. Therefore, the analysis of the axle box bearing signal becomes a meaningful and challenging topic.

To date, there are two popular fields which have been intensively researched for employing on rotational machinery fault diagnosis. One is to extract the resonance band of the impulse excited by the local or distribution defect of machinery, including empirical mode decomposition (EMD) [6], empirical wavelet transformation (EWT) [7], fast kurtogram [8], and variational mode decomposition (VMD) [9]. The purpose of this type of method is to narrow the analyzed frequency band and to help the further processes to perform better. Another kind of approaches, such as envelope analysis [10], squared envelope analysis [11], fast spectral correlation [12], and cyclostationary analysis [13], focus on demodulating or revealing the faulty signal pattern based on the assumption that the impulses excited by the defect are generally considered as an amplitude modulated and quasiperiodic signal.

As an alternative approach, the morphological filter (MF) has brought some discussion on bearing fault

diagnosis in recent years. The morphological filter is essentially an incorporation of nonlinear signal operators, design methodology, and application related to mathematical morphology [14]. According to the theory of mathematical morphology, the analyzed signal is considered as a set in a Euclidean space. The MF is viewed as a set operation that transforms the graph of the analyzed signal, which provides a quantitative description of its geometrical characteristics. The MF was first used in analyzing binary and grey-level images and then applied in periodic signals by Nikolaou as an envelope-type signal processing tool [15]. The typical response pattern of periodic impacts excited by bearing defects comprises an amplitude modulation. Since the vibration signal is in the form of vibration amplitude with respect to time, MF can be considered as a nonlinear 1D signal processing tool. The idea of MF is to construct a data set, called structural element (SE), and to design morphological operators to modify the shape of the analyzed signal so that the period impulse excited by the rotation machinery defect can be demodulated from the analyzed signal [16]. In early MF researches, single-scale MF with fixed SE parameter was generally adopted. This method suffered from some shortages, including the requirement of prior knowledge and the incomplete extraction of pulse characteristics [17]. Later, in order to improve the performance of MF, multiple-scale MF was introduced based on the concept of optimization from MF results with various SE parameters. Several research studies apply various types of MF operators to approach the bearing fault diagnosis [18–20], but it appears that different MF operators would produce various effects on different bearing vibration signals because of the various interference noises. Moreover, the construction of SE is another significant factor that affects the performance of MF. It would be complicated and time consuming to simultaneously select the optimal MF operator and SE when applying MF on new bearing fault signals.

Therefore, a novel method combining MF and an optimizing method called particle swarm optimization (PSO) is proposed in this paper. PSO is one of the popular optimization algorithms [21–23], which finds the optimal solution through information sharing among a group of independent individuals. PSO has been broadly applied in many fields especially in high-dimensional optimization problems [24]. By applying PSO on MF, the selection of the optimal MF operators and SE parameters could be more applicable and less time consuming. The idea of the proposed method is to build up a selecting scheme to overall consider the performance of numerous operators and select the best MF operator and SE to extract the optimal fault pattern in bearing signals. Moreover, to verify the effectiveness of the proposed method, several measured bearing fault signals with strong interference were analyzed in this paper.

The remaining contents of this paper are organized as follows: the principles of MF and PSO are simply recalled in Section 2; the detail and procedures of the proposed method are introduced in Section 3; the simulation signal is analyzed by the proposed method in Section 4; then, some vibration signals of the axle box of the railway vehicle are provided to verify the effectiveness of the proposed method; finally, the summary is drawn in the last section.

2. Theoretical Background

2.1. Morphological Filter. The morphological filter is a pure time-based and nonlinear signal-processing method, which modifies the shape of the analyzed signal via the interaction with the structure element (SE). The MF operator is one of the key factors that affects the filtering performance, which designates the interaction pattern between SE and the analyzed signal. For a one-dimensional signal, the two very basic MF operators are called dilation and erosion. Let $f(n)$ be an original 1D signal which ranged in the domain $F = (0, 1, 2, \ldots, N-1)$, and an SE indicated by $g(m)$ in the domain $G = (0, 1, 2, \ldots, M-1)$. The expressions of dilation and erosion are formulated as follows:

$$\begin{aligned}(f \oplus g)(n) &= \max[f(n-m) + g(m)],\\ (f \ominus g)(n) &= \min[f(n-m) + g(m)],\end{aligned} \tag{1}$$

where $n \in F$ and $m \in G$ and $\oplus$ and $\ominus$ indicate the dilation and erosion respectively. Based on the two operators above, another two basic operators, called opening and closing, are further defined as follows:

$$\begin{aligned}(f \circ g)(n) &= (f \ominus g^{-} \oplus g)(n),\\ (f \bullet g)(n) &= (f \oplus g^{-} \ominus g)(n),\end{aligned} \tag{2}$$

where $g^{-}(n) = g(-n)$ and $\circ$ and $\bullet$ represent opening and closing separately. The basic operators of MF comprise the four operators above. However, it is apparent that the MF cannot fully meet the requirements of nonlinear signals by only applying these basic operators. Therefore, more operators are proposed to extend the flexibility of MF, and in this paper, some classical MF operators, which have been commonly used, are collected and listed in Table 1 [25, 26]. For the sake of briefness, only the names and expressions of these operators are shown.

On the other hand, SE roles as a geometric detector to match and unify the shape of the analyzed signal. According to the operator expression mentioned above, the outcome of MF also depends on the construction of SE. The desired waveform can be extracted properly only when the shape and size of SE are matched with the analyzed signal. Therefore, the parameters, including the shape, length, and height in the 1D signal case, are decisive for the performance of MF.

The most commonly used shapes of SE are flat and triangle for a 1D signal. The construction of these SEs is shown in Tables 2 and 3. Apparently, the length affects the construction of both flat and triangle SEs, while the height is another important parameter to construct a triangle SE.

2.2. Particle Swarm Optimization. Particle swarm optimization (PSO) is a popular global optimization algorithm that

Table 1: The classical operations and corresponding expressions.

Name	Expression	Name	Expression
Morphological gradient (MG)	$(f \oplus g)(n) - (f \Theta g)(n)$	Difference filter (DIF)	$(f \bullet g)(n) - (f \circ g)(n)$
Black top-hat transform (BTH)	$(f \bullet g)(n) - f(n)$	Close and open average ($A_{C\&O}$)	$((f \bullet g)(n) + (f \circ g)(n))/2$
White top-hat transform (WTH)	$f(n) - (f \circ g)(n)$	Open-close (OC)	$(f \circ g \bullet g)(n)$
Combination of WTH and positive BTH ($C_{WTH\&PBTH}$)	$2f(n) - (f \circ g)(n) - (f \bullet g)(n)$	Close-open (CO)	$(f \circ g \bullet g)(n)$
Combination morphological filter (CMF)	$((f \bullet g \circ g)(n) + (f \circ g \bullet g)(n))/2$	CO and OC gradient ($G_{CO\&OC}$)	$(f \bullet g \circ g)(n) - (f \circ g \bullet g)(n)$
Combination morphological filter hat (CMFH)	$f(n) - (((f \bullet g \circ g)(n) + (f \circ g \bullet g)(n))/2)$	Morphology gradient product operation (MGPO)	$[(f \bullet g)(n) - (f \circ g)(n)] \cdot [(f \bullet g \circ g)(n) - (f \circ g \bullet g)(n)]$

Table 2: The construction of flat SEs.

Scale	Length	Matrix form
1	2	{0, 0}
2	3	{0, 0, 0}
3	4	{0, 0, 0, 0}
n	$n+1$	{0, 0, . . ., 0, 0}

Table 3: The construction of triangle SEs.

Scale	Length	Matrix form
1	3	h_1{0, 1, 0}
2	5	h_2{0, 1, 2, 1, 0}
3	7	h_3{0, 1, 2, 3, 2, 1, 0}
n	$2n+1$	h_n{0, 1, . . ., n, . . ., 1, 0}

was inspired by the social activities of birds' foraging. PSO builds up a set of articles with two properties named position and velocity which represent the direction and velocity of the particles' self-movement, respectively. In the meanwhile, each particle iteratively explores for the optimal solution within its own search domain and shares the individual optimal position with other particles in each iteration level. According to the information gathered from particles, the current optimal positions and velocity would be updated and fed back to the corresponding particle. The detailed process of PSO is introduced as follows:

Step 1. Initialize a group of particles with random positions and velocities. Then, calculate the initial fitness value of each particle.

Step 2. Record the initial position as the current optimal position of each particle and the best position among the particles as the global optimal position. The individual optimal position is marked as $p_{n,1}$ where n indicates the nth particle; and the global optimal position is recorded as g_1.

Step 3. According to the current individual optimal position and the global optimal position, the velocity $v_{n,i}$ of each particle is updated, where i indicates the number of iteration. The update follows the pattern defined as follows:

$$v_{n,i} = \omega v_{n,i} + c_1 r_1 \left(p_{n,i} - x_{n,i}\right) + c_2 r_2 \left(g_i - x_{n,i}\right), \quad (3)$$

where ω is called as inertia factor, c_1 and c_2 are the learning factors, and r_1 and r_2 are the random numbers valued within [0, 1].

Step 4. After obtaining the updated velocity $v_{n,i}$, the positions of particles are adjusted as follows:

$$x_{n,i} = x_{n,i-1} + v_i. \quad (4)$$

Step 5. Calculate the fitness values and compare with the values of the former level. Then, update $p_{n,i}$ and g_i according to the particles with the best fitness value.

Step 6. Repeat Step 3 to Step 5 until the fitness values are satisfied or the iteration level meets the limitation.

3. Morphological Filter Based on Particle Swarm Optimization

Taking the superior optimizing capability of PSO, the selection of the MF operator and SE can be converted to a parameter optimizing problem. Therefore, a morphological filter based on particle swarm optimization (named PSO-MF in this paper for simplicity) was proposed in this paper. Before introducing the procedures of PSO-MF, some considerations about the combination of PSO and MF should be explained.

Firstly, taking into account the time lag among the impulses excited by the bearing defect is relatively short, especially in high-operation speed (i.e., high shaft rotation speed), the adequate length of a semicircular SE has a high possibility to cover more than one impulse of defect; therefore, the semicircular shape is not suitable for our cases. The triangle SE is similar as the flat SE when the height approximates or equals to zero; hence, the form of triangle SE was applied in the proposed method so that two shapes of SE could be considered.

Secondly, the position of original PSO is incapable to represent the operators, SE length and SE height simultaneously, so the dimensions of PSO are defined as types of operators so that each dimension is corresponding to one

MF operator. Moreover, the position of a particle in PSO-MF contains two parameters which are the height and length of SE with different domain, respectively.

Thirdly, considering the periodicity and pseudostationarity of the faulty bearing signal, the kurtosis, which has been widely used in bearing diagnosis, is applied as the index of fitness value of PSO-MF. The kurtosis is an index to reflect the distribution characteristic of data sets [27]. Generally, with higher kurtosis value, the signal is reckoned as carrying more periodical information in the aspect of processing the bearing signals [28].

According to the discussions above, the procedures of PSO-MF are defined as follows:

Step 1. Construct the multiple-dimension particle swarm. The MF operator of each dimension is expressed as

$$\mathrm{MF}_d = [f, g(h,l)]^d_{\mathrm{MF}}, \tag{5}$$

where d indicates the dth dimension (i.e., operator), $[\cdots]_{\mathrm{MF}}$ represents the corresponding MF operator, and $g(h,l)$ is the SE with a height of $h \in [0,3]$ and length of $l \in [2, 0.6\,T]$, in which T is the theoretical time lag between two impulses excited by the bearing defect.

Step 2. Randomize the value of the properties of each particle; then, calculate the initial fitness value according to the kurtosis formulation in the following equation:

$$\mathrm{Kurtosis} = \frac{\sum (x(t) - \mu_x)^4}{\left[\sum (x(t) - \mu_x)^2\right]^2}, \tag{6}$$

where μ_x indicates the mean value of the data set. The initial positions of each particle are recorded as $p^d_{n,1}$, and the positions of the particle with the maximum kurtosis in each dimension are recorded as g^d_1, where $n = 1, 2, \ldots, N$ and N indicates the swarm size. In this paper, the swarm size is assigned as 20.

Step 3. Introduce $p^d_{n,i}$ and g^d_i into equation (3) to obtain a new update pattern of particle velocity as follows:

$$v^d_{n,i} = \omega v^d_{n,i} + c_1 r_1 \left(p^d_{n,i} - x^d_{n,i}\right) + c_2 r_2 \left(g^d_i - x^d_{n,i}\right), \tag{7}$$

and update the position of each particle:

$$x^d_{n,i} = x^d_{n,i} + v^d_{n,i}, \tag{8}$$

where $i = 1, 2, \ldots, I$ in which I is the iteration number, which in the proposed method is valued as 100. In addition, the learning factors and inertia factor are primary for the computation cost of PSO, but the effects on the final result of PSO-MF are limited. In the proposed method, the parameter values follow the choice in the literature [29], where $c_1 = c_2 = 0.72$ and $\omega = 1.19$.

Step 4. Calculate the kurtosis of MF operations with each particle, and then compare with values of the former level. Update $p^d_{n,i}$ and g^d_i according to the particle with the largest kurtosis.

Step 5. After repeating step 3 and 4 until the iteration meets the limitation, the best solutions of each dimension will be obtained. Select the dimension with the largest kurtosis as the final output of PSO-MF.

Step 6. Apply the operator and SE selected by PSO-MF to the bearing faulty signal, and then observe its waveform or frequency spectrum if necessary.

In order to make a clearer view of the proposed method, the flowchart of PSO-MF is illustrated as shown in Figure 1.

4. Simulation

The actual systems of rotation machinery are normally suffered from various known or unknown interference resulting in lots of signal components that cannot be well explained. Therefore, a simulated bearing faulty vibration signal was firstly constructed to verify the effectiveness of PSO-MF with certain signal components. The simulated signal is expressed as follows:

$$s(t) = s_1(t) + s_2(t) + s_3(t) + \eta, \tag{9}$$

where s_1 represents a shaft-rotational interference transmitted from wheel-track excitement, s_2 and s_3 are formed as impulses excited by an outer-race defect at different resonance frequency, and η is a white Gaussian white noise with a signal-noise ratio of -5 dB. The formulation of s_n is the impulse response of a single degree of freedom mass-spring-damper:

$$s_n(t) = A_n e^{-\beta_n t} \sin \omega_n(t) u(t), \tag{10}$$

where A indicates the amplitude of impulse, β is the coefficient of structural damping, ω indicates the resonance frequency of the impulse, and $u(t)$ represents the response of unit step. The resonance frequencies of s_1, s_2, and s_3 are set as 500 Hz, 2000 Hz, and 3500 Hz, respectively, and the frequencies of shaft rotation and outer-race fault are 10.29 Hz and 83.33 Hz. In addition, slight noises of 10 dB are separately added in s_1, s_2, and s_3 as the interference of signal collecting systems. Figure 2 illustrates the waveforms of s_1, s_2, and s_3, and the amplitude of s_1 is assigned as the largest since the impulses from the wheel-track are generally dominant.

The waveform, frequency spectrum, and envelope spectrum of $s(t)$ are depicted in Figure 3. The impulses excited by the wheel-track can be found clearly from the waveform. However, the impulses of the bearing defect are blurred. By observing the envelope spectrum, the frequency of shaft rotation and its corresponding harmonics are dominant, while the fault frequency and its 2^{nd}–4^{th} order harmonics can be detected under the interference of shaft rotation and noise.

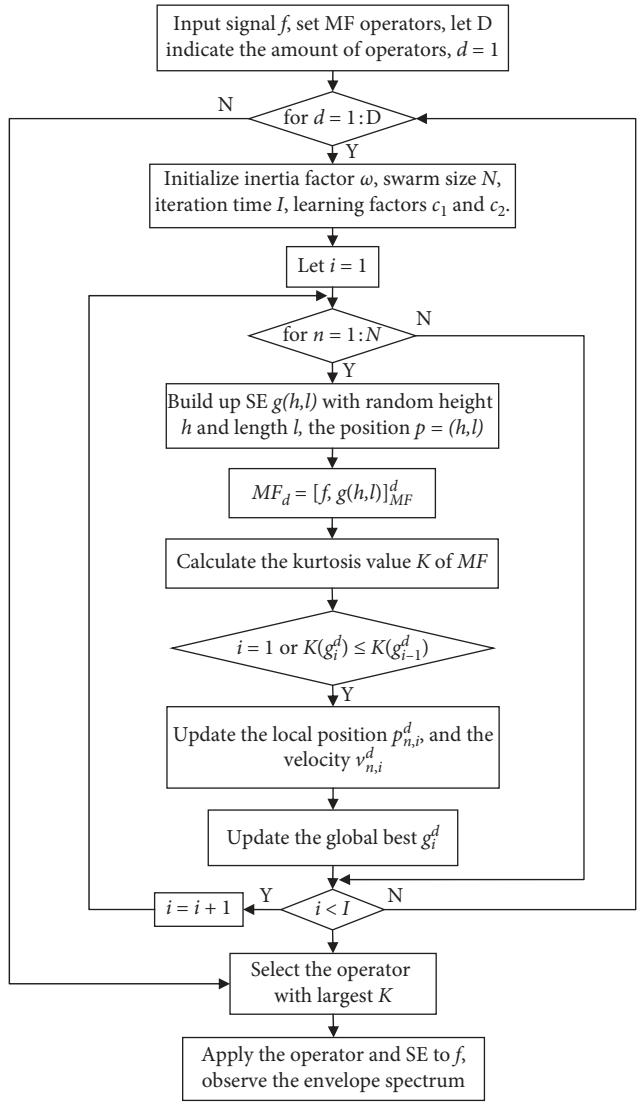

Figure 1: Flowchart of proposed PSO-MF on the bearing fault signal.

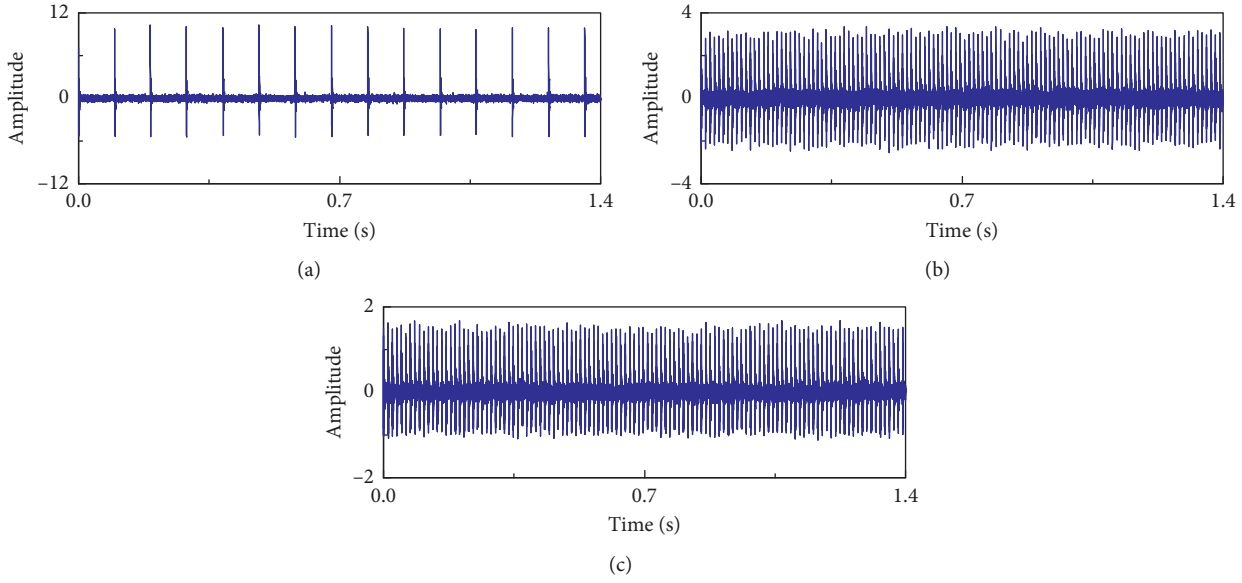

Figure 2: Waveforms of simulated signals: (a) s_1, (b) s_2, and (c) s_3.

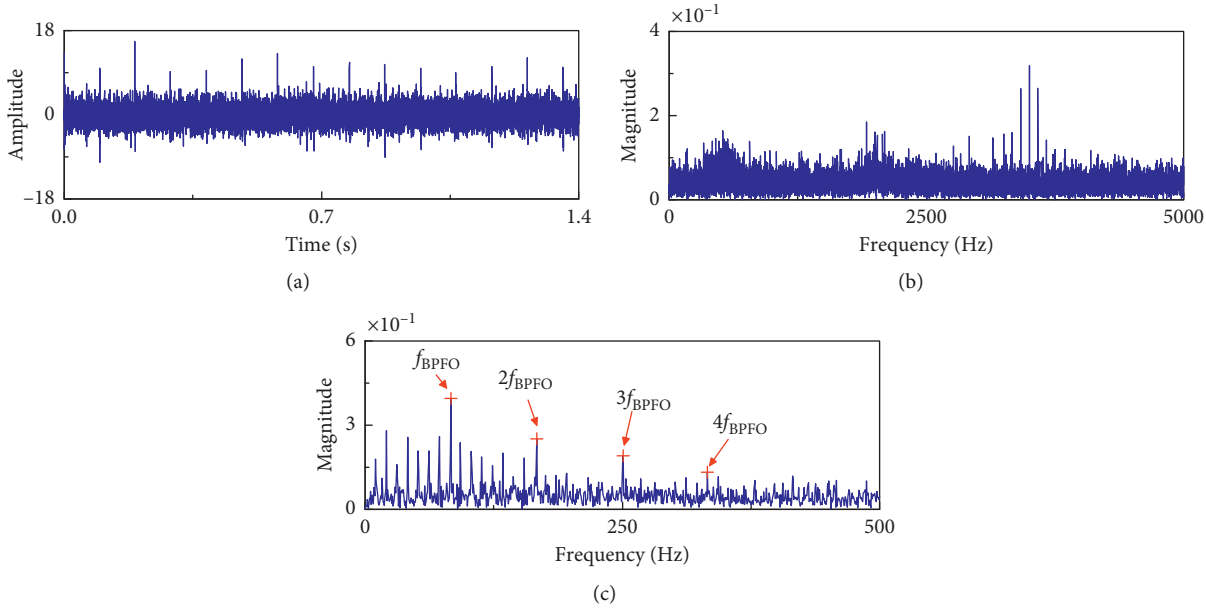

Figure 3: The time-domain and frequency-domain of the simulation signal: (a) the waveform, (b) the spectrum, and (c) the envelope spectrum.

After applying PSO-MF to the simulated signal, the optimized SE parameters of each operator are obtained and the outputs of the operators are calculated according to equation (6). Table 4 lists the kurtosis of the operators. The operator (in this case, BTH) with highest kurtosis among operators is regarded as the optimal solution. Since the operations of MF are purposed variously, we only collected 16 typical operators in the proposed method in this paper.

The optimal results of the collected operators are shown separately in Figure 4. According to Figure 4, six operations (including MG, DIF, BTH, WTH, GCO&OC, and MGPO) are capable of detecting the fault characteristic frequency with well performance. Others either have strong interference or fail to reveal the fault frequency. In this simulation case, the operator selected by the proposed method is BTH, which is one of the best performed operators that efficiently extracts the fault frequency and its harmonics.

In this simulation case, the output of PSO-MF is one of the best-performing operators. It tentatively proves that the proposed method effectively selects the best solution among several operators and their corresponding SE (certain operators with equal performance may coexist, but it is no need to recognize them entirely). In order to further testify the performance of the proposed method, a set of measured data were used in the next chapter.

Table 4: The kurtosis values of collected operations of the simulated signal.

Operator	Kurtosis
Dilation	13.63
Morphological gradient (MG)	14.64
Open	2.98
Difference filter (DIF)	14.74
White top-hat transform (WTH)	28.88
Close-open (CO)	9.68
Combination morphological filter (CMF)	3.95
Combination morphological filter hat (CMFH)	19.49
Erosion	4.59
Close	13.45
Close and open average ($A_{C\&O}$)	4.97
Black top-hat transform (BTH)	29.79
Combination of WTH and positive BTH ($C_{WTH\&PBTH}$)	11.38
Open-close (OC)	2.78
CO and OC gradient ($G_{CO\&OC}$)	15.03
Morphology gradient product operation (MGPO)	22.02

5. Experiment: Fault Diagnosis for Axle Box Bearing

The experiment of this paper was conducted on a running rig by Southwest Jiaotong University (SWJTU) and CRRC Corporation. The test rig is shown in Figure 5(a). The axle box supported the tested wheel set during the operation and was forced by a statical load. The accelerator was mounted on the surface of the axle box as shown in Figure 5(b). Two types of bearing defect, including outer race and rolling element fault, were manually made as demonstrated in Figures 5(c) and 5(d). The type of railway vehicle bearing is generally adopted by double-row tapered roller bearing; therefore, the inner-race fault is difficult to be made without heavily damaging the bearing. Alternatively, the inner-race faulty data conducted by Case Western Reserve University (CWRU) was applied in our experiment (the data set has been widely researched and the

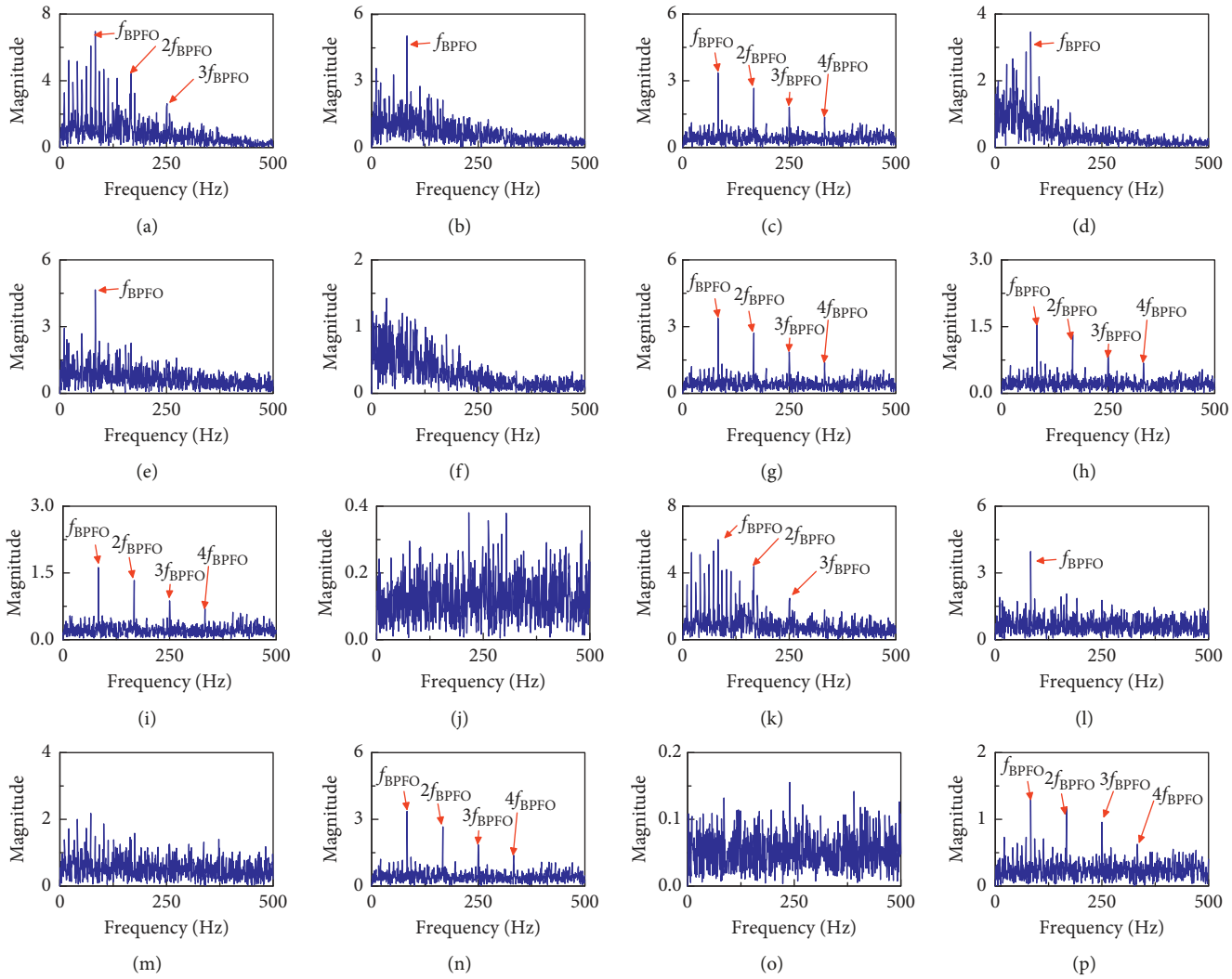

FIGURE 4: The spectra of collected operations of the simulated signal. (a) Dilation. (b) Erosion. (c) MG. (d) Close. (e) Open. (f) $A_{C\&O}$. (g) DIF. (h) BTH. (i) WTH. (j) $C_{WTH\&PBTH}$. (k) Close-open. (l) Open-close. (m) CMF. (n) $G_{CO\&OC}$. (o) CMFH. (p) MGPO.

details of the test rig can be referred from [30, 31]). Moreover, the vibration environment of the test rig is simpler than the practical operation, while conducting an experiment of faulty bearing in practical operation is dangerous for passengers and extraordinarily costly. Alternatively, a set of normal data, measured from the axle box of a CRH vehicle during the actual operation, was added on the test rig data as an addition colored noise from the wheel-track system. The sampling frequency of the signal from CWRU is 12 kHz, while the signal from SWJTU and practical operation are both sampled by 10 kHz. The signal from CWRU was downsampled to 10 kHz when synthesizing the inner-race fault and actual operating signal.

The theoretical calculations of the characteristic frequencies of outer race, inner race, and rolling element are expressed as follows [32]:

$$f_{BPFO} = \frac{Zf_r}{2}\left(1 - \frac{d}{D}\cos\alpha\right),$$
$$f_{BPFI} = \frac{Zf_r}{2}\left(1 - \frac{d}{D}\cos\alpha\right), \quad (11)$$
$$f_{BSF} = \frac{Df_r}{2d}\left(1 - \left(\frac{d}{D}\cos\alpha\right)^2\right),$$

where f_r is the shaft rotating frequency and Z, d, D, and α indicate the rollers number, roller diameter, pitch diameter, and angle of contact, respectively. The working condition and corresponding fault frequency are listed in Table 5. Note that the speed of the inner-race case is an approximation speed according to the wheel diameter ratio of the signal from SWJTU.

Table 5: Fault characteristic frequencies of tested bearing.

Defect type	Speed (Km/h)	Motor speed (rpm)	Shaft rotation frequency (Hz)	Fault characteristic frequency (Hz)
Rolling element	50	308	5.14	16.82
Outer race	100	616.88	10.28	83.26
Inner race	280	1730	28.83	156.12

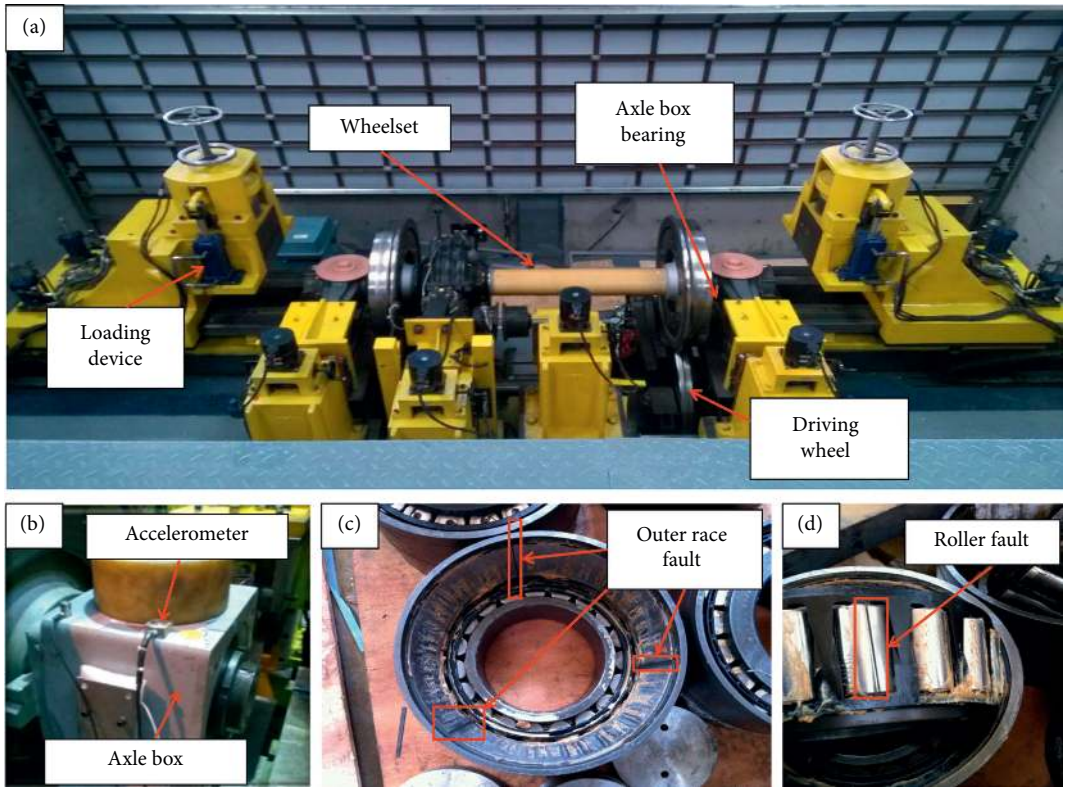

Figure 5: Photos of the bearing test rig from SWJTU: (a) the test rig, (b) the installation of the sensor, (c) the defect of outer race, and (d) the defect of rolling element.

In the following experimental cases, the frequency spectra of all operators will be demonstrated to testify the effectiveness of the proposed selecting scheme. Moreover, three popular diagnostic methods, including envelope analysis (EA), enhance envelope spectrum (EES) and autocorrelation spectrum (AC), are applied to compare with the performance of the proposed method.

5.1. The Case of Outer-Race Fault. The first experiment case is using the data collected from the bearing with outer-race fault. The data collected from actual operation (called operating signal in this paper for brevity) are segmented from the data with a uniform speed of 78 km/h to approximately match the speed of the testing rig (due to the limitation of the field-experimental conditions, the speed is the most approximate uniform velocity to 100 km/h). Figure 6 demonstrates the waveforms of operating signal, testing data, the synthesized signal, and its corresponding frequency spectrum. There is a dominant frequency of 50 Hz in Figure 6(d) known as the power frequency. Moreover, three resonance bands could be roughly observed of which the low-frequency band seems to be more dominant.

After applying the PSO-MF to the synthesized data, the kurtosis of the optimal solutions of each operator was obtained and recorded as shown in Table 6. The output of the PSO-MF in this case is the BTH. The frequency spectra of the filtered signals are demonstrated in Figure 7. Most of the operators failed to extract the fault frequency except MG, DIF, BTH, and WTH. MG and BTH have the best envelope performance by the evidence of the clearer harmonic frequency. It is indefinite to evaluate the better performance between MG and BTH since the relative amplitude of the 1st harmonic of BTH is slightly higher than MG; however, the interference noise of MG is relatively lower. Therefore, the performances of MG and BTH are regarded as equivalent.

After the optimal solution was acquired via PSO-MF, the spectra, illustrated in Figure 8, of other signal processing methods mentioned above were conducted. The envelope spectrum is shown in Figure 8(b), of which harmonics of faulty frequency are vaguely observed. The enhanced envelope spectrum and autocorrelation spectrum have better

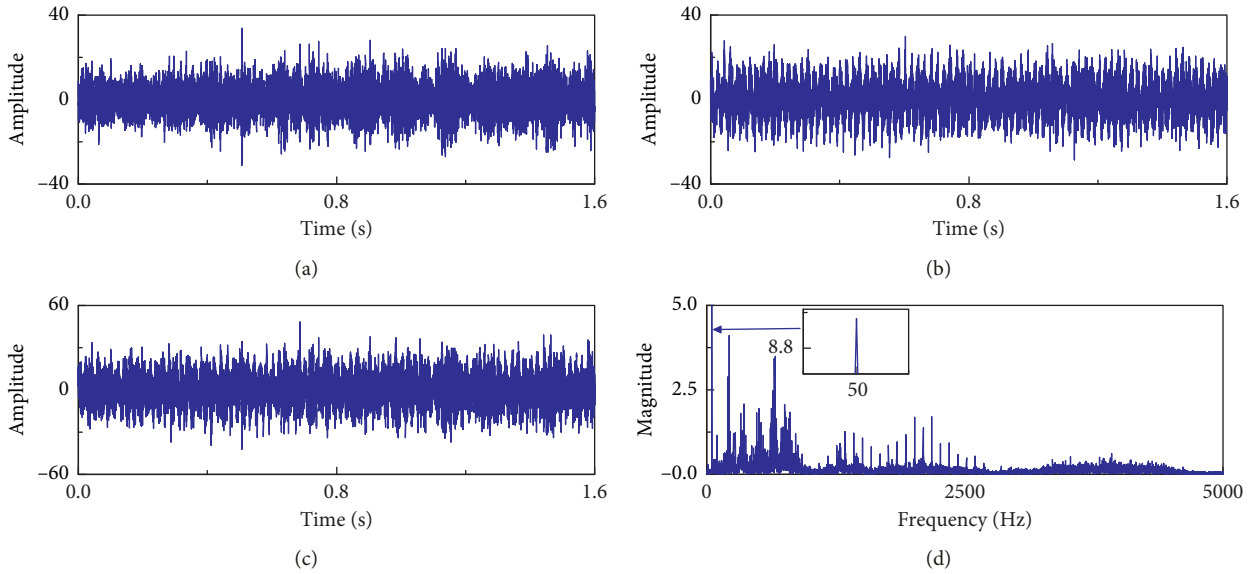

Figure 6: The outer-race fault signal and operating signal: (a) the waveform of operating signal, (b) the waveform of test rig signal, (c) the waveform of synthesized signal, and (d) the spectrum of synthesized signal.

Table 6: The kurtosis values of collected operations of the outer-race fault signal.

Operator	Kurtosis
Dilation	1.33
Morphological gradient (MG)	2.61
Open	1.13
Difference filter (DIF)	2.76
White top-hat transform (WTH)	3.38
Close-open (CO)	0.86
Combination morphological filter (CMF)	0.94
Combination morphological filter hat (CMFH)	2.33
Erosion	1.02
Close	1.07
Close and open average ($A_{C\&O}$)	0.98
Black top-hat transform (BTH)	6.39
Combination of WTH and positive BTH ($C_{WTH\&PBTH}$)	1.32
Open-close (OC)	0.98
CO and OC gradient ($G_{CO\&OC}$)	3.01
Morphology gradient product operation (MGPO)	4.56

performance than the envelope spectrum because of the more obvious harmonics and the revelation of the 4th harmonic. The outcome of PSO-MF is undoubtedly the best extraction of the fault information due to the clear and sufficient detection of the fault frequency and its corresponding harmonics. Therefore, in this case, PSO-MF is testified to realize the fault information more accurately and efficiently comparing with the other three methods.

5.2. The Case of Rolling Element Fault. The data of rolling element were secondly analyzed by PSO-MF. The speed of the operating signal is 58 Km/h which is as close as possible to the speed of the test rig. The waveforms of the operating signal, testing data, and synthesized data are depicted as shown in Figure 9(a)–9(c). The spectrum of the synthesized signal is shown in Figure 9(d) which suffered from the same power frequency interference as the outer-race faulty signal. After exploiting PSO-MF to the faulty signal, the kurtosis values of each dimension are listed in Table 7. The operator with the highest kurtosis is BTH which is marked by blue shading.

The spectra of the MF operations are illustrated in Figure 10. The rolling elements spin with the rotation of the bearing cage during the bearing operation, and the frequency of the rolling element defect is modulated by the frequency of the bearing cage. The frequency of the bearing cage is normally much less than the frequency of the rolling element; therefore, the spectrum of the rolling element normally presents as the frequency families which consisted of the fault frequency and the frequencies spaced at the cage rotational frequency. According to Figure 10, the effective operators are MG, DIF, BTH, and WTH where the red dot circles represent the frequency families of the rolling element fault. Among these operators, the performance of WTH is slightly worse than other effective operators since some fault frequency families are relatively indistinct. The selection of PSO-MF (BTH) is one of the well-performed operators, which verified the effectiveness of the proposed optimizing scheme.

Figure 10 shows the spectra of PSO-MF, envelope, enhance envelope, and autocorrelation, respectively. The spectrum of PSO-MF is zoomed in as shown in Figure 11(a) where the red rectangles indicate the frequency of the bearing cage. Note that the harmonics of the rolling element passing frequency are appeared double the theoretical frequency since the rolling element defect generates two impulses by impacting both inner and outer in a single rotation period. It is obvious that the envelope spectrum, enhanced envelope spectrum, and autocorrelation spectrum are failed to recognize the pattern of the rolling element defect under

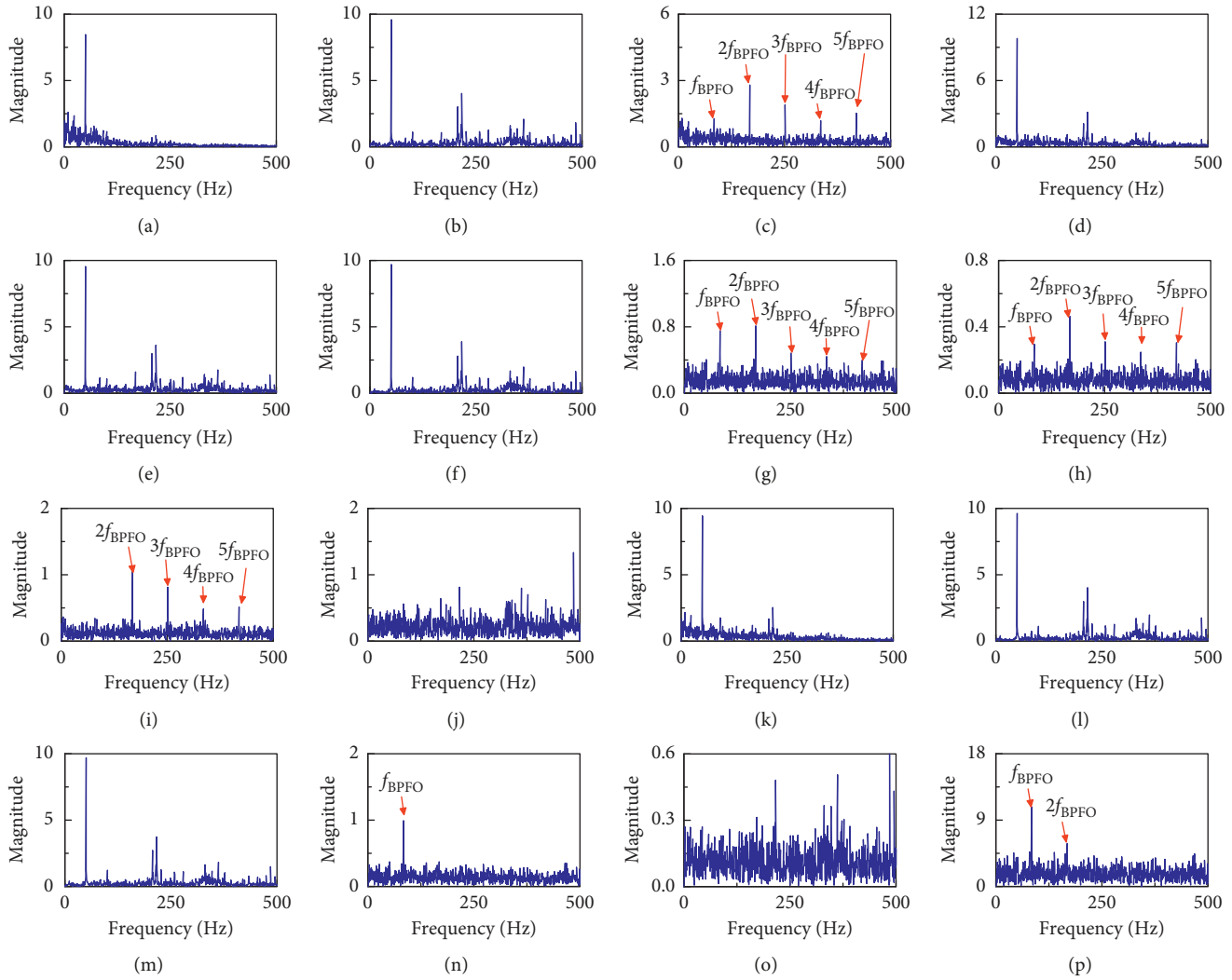

FIGURE 7: The spectra of collected operations of the outer-race fault signal. (a) Dilation. (b) Erosion. (c) MG. (d) Close. (e) Open. (f) $A_{C\&O}$. (g) DIF. (h) BTH. (i) WTH. (j) $C_{WTH\&PBTH}$. (k) Close-open. (l) Open-close. (m) CMF. (n) $G_{CO\&OC}$. (o) CMFH. (p) MGPO.

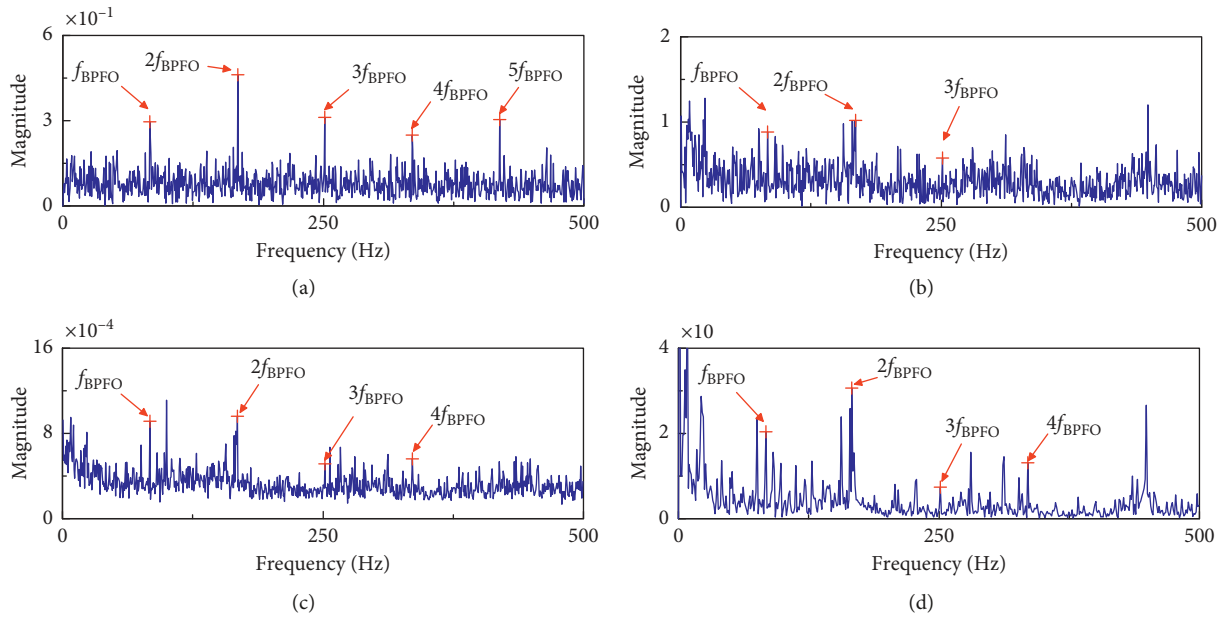

FIGURE 8: The spectra of comparison methods of the outer-race fault signal: (a) PSO-MF, (b) envelope spectrum, (c) enhanced envelope spectrum, and (d) autocorrelation spectrum.

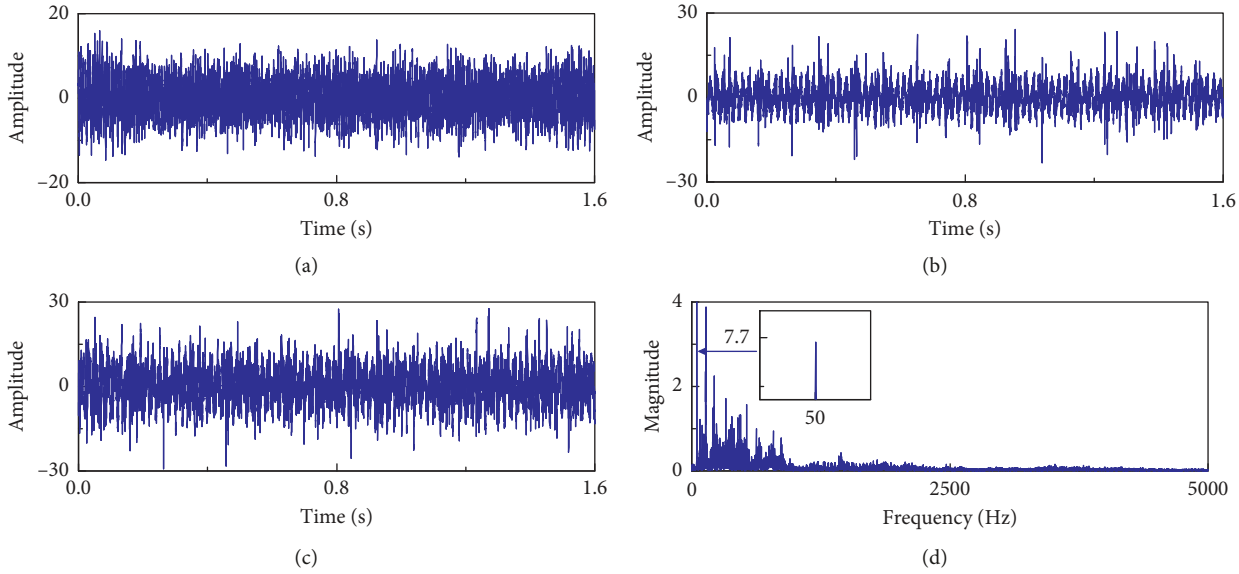

Figure 9: The rolling element fault signal and operating signal: (a) the waveform of the operating signal, (b) the waveform of the test rig signal, (c) the waveform of the synthesized signal, and (d) the spectrum of the synthesized signal.

Table 7: The kurtosis values of collected operations of the rolling element fault signal.

Operator	Kurtosis
Dilation	1.88
Morphological gradient (MG)	33.28
Open	1.19
Difference filter (DIF)	53.37
White top-hat transform (WTH)	64.62
Close-open (CO)	0.66
Combination morphological filter (CMF)	1.06
Combination morphological filter hat (CMFH)	24.88
Erosion	2.12
Close	1.22
Close and open average ($A_{C\&O}$)	1.09
Black top-hat transform (BTH)	119.38
Combination of WTH and positive BTH ($C_{WTH\&PBTH}$)	35.23
Open-close (OC)	1.18
CO and OC gradient ($G_{CO\&OC}$)	43.63
Morphology gradient product operation (MGPO)	3.66

the heavy interference of power frequency and wheel-track excitement.

5.3. The Case of Inner-Race Fault. The third case is the inner-race data from CWRU. The speed of the operating signal is 246 km/h. The waveforms are shown in Figure 12 since the interference of the test data is extremely low, and the amplitude of the operating signal is adjusted to be overwhelming. The spectrum of the synthesized data is shown in Figure 12(d).

After processing PSO-MF to the faulty signal, the kurtosis values of the collected operators were obtained as presented in Table 8. The output of PSO-MF in this case is WTH. The corresponding optimization outputs of each operator are illustrated in Figure 13, where the red triangles indicate the frequency modulated by rotation frequency. It can be found that MG, DIF, BTH, WTH, and $G_{CO\&OC}$ are capable of revealing the inner-race fault pattern. The output of PSO-WTH is WTH, which appears as the most sufficient pattern with clearest characteristic and modulated frequencies.

The further comparisons among EA, EES, and AC are shown in Figure 14. Figure 14(a) shows the zoom-in spectrum of the output of PSO-MF, and the inner-race frequency and its harmonics can be observed clearly. Moreover, since the inner-race defect spins with the shaft rotation, frequencies modulated by shaft rotation, appear around the fault frequency spacing at the shaft rotation frequency, are exposed by PSO-MF distinctly. On the contrary, the envelope spectrum, enhanced envelope spectrum, and autocorrelation spectrum are incapable of realizing the fault information under the overwhelming interference of the operating signal.

6. Discussion

6.1. The Selection and Performance of the Collected Operators. To date, the operators and shapes of SE are variously proposed and testified in many researches, which make the full collection of all operators become extremely difficult and time consuming. The intention of the proposed method is to build up a scheme to solve the choosing problem for each certain signal; hence, only some typical operators are selected. It is acceptable and applicable to add some emerging operators into the proposed method which may hopefully improve the effect of MF. As claimed in the introduction, different operators may fit for different types of signals and the best operator for all faulty signals barely exists. In our cases, some operators (such as morphological gradient, black top-hat, white top-hat, and difference filter)

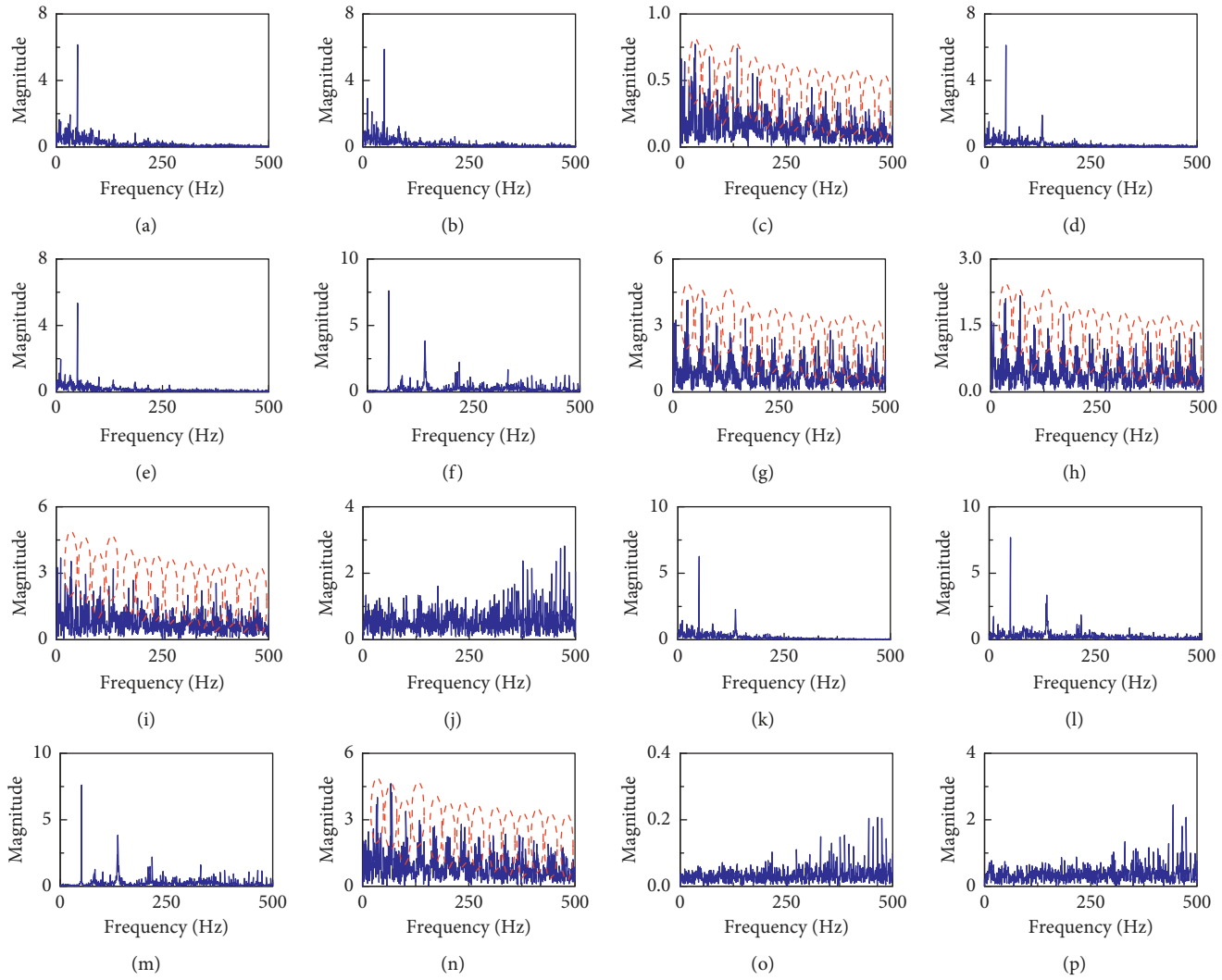

FIGURE 10: The spectra of collected operations of the rolling element fault signal. (a) Dilation. (b) Erosion. (c) MG. (d) Close. (e) Open. (f) $A_{C\&O}$. (g) DIF. (h) BTH. (i) WTH. (j) $C_{WTH\&PBTH}$. (k) Close-open. (l) Open-close. (m) CMF. (n) $G_{CO\&OC}$. (o) CMFH. (p) MGPO.

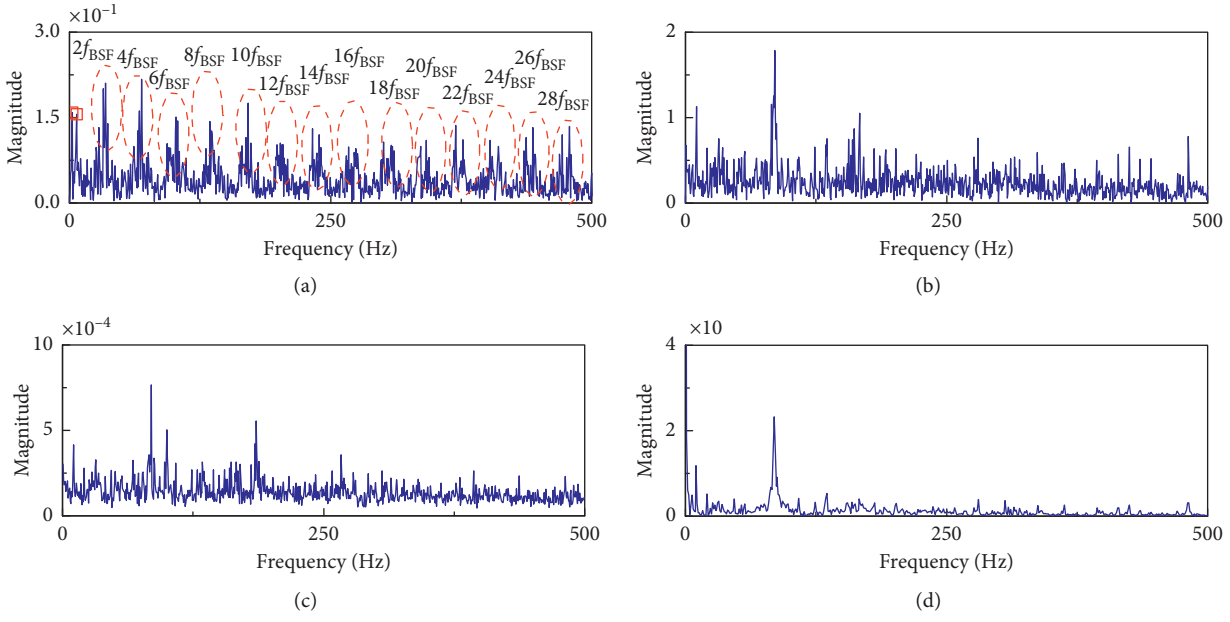

FIGURE 11: The spectra of comparison methods of the rolling element fault signal: (a) PSO-MF, (b) envelope spectrum, (c) enhanced envelope spectrum, and (d) autocorrelation spectrum.

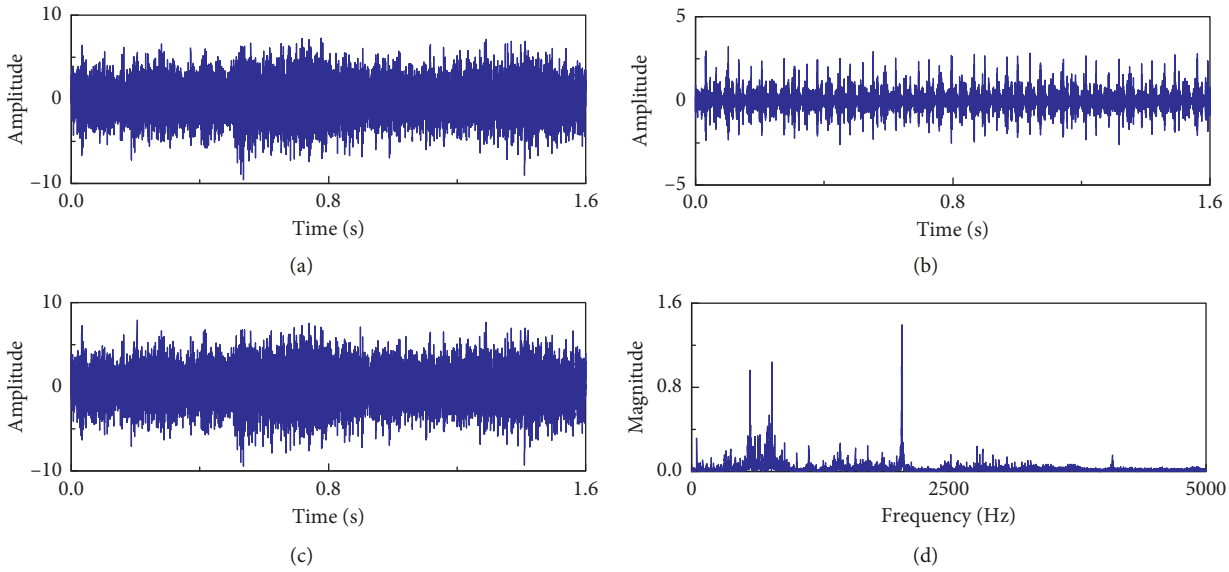

Figure 12: The inner-race fault signal and operating signal: (a) the waveform of the operating signal, (b) the waveform of the test rig signal, (c) the waveform of the synthesized signal, and (d) the spectrum of the synthesized signal.

Table 8: The kurtosis values of collected operations of the inner-race fault signal.

Operator	Kurtosis
Dilation	1.19
Morphological gradient (MG)	15.65
Open	1.69
Difference filter (DIF)	14.65
White top-hat transform (WTH)	32.07
Close-open (CO)	1.05
Combination morphological filter (CMF)	1.16
Morphology gradient product operation (MGPO)	3.56
Erosion	1.96
Close	1.90
Close and open average ($A_{C\&O}$)	1.18
Black top-hat transform (BTH)	26.71
Combination of WTH and positive BTH ($C_{WTH\&PBTH}$)	15.06
Open-close (OC)	1.61
CO and OC gradient ($G_{CO\&OC}$)	12.90
Combination morphological filter hat (CMFH)	15.06

are stably effective and some operators (CO&OC gradient and morphology gradient product operation) are mostly functional while some operators do not work for the data. Note that the outputs shown in Figures 4, 7, 10, and 13 are not sufficient to judge the performance of these operators but only the support the PSO-MF when dealing with different bearing fault signals.

6.2. The Phase and Speed of Operating Signal. There are some constraints in the field test of the operating vehicle, so the uniform operating speed is hard to perfectly match the speed of the testing rig. The different speed will cause the difference of phase in a signal with limited length. However, according to the analyses in our experiments, the intervention of the operating signal does not eliminate the pattern of bearing faults but only raises the difficulty for diagnosing. Considering the phase difference, the operating signals containing wheel-track excitement are added as a set of colored noise; therefore, the corresponding analyses of operating signals were neglected so that the revelation of fault patterns can be more highlighted in this paper.

7. Conclusion

In this paper, to improve the performance of the morphological filter on diagnosing defects of railway vehicle bearing, the morphological filter based on particle swarm optimization was proposed. The main idea of the proposed method is firstly setting multiple dimensions to represent some typical operators and searching the optimal solutions of each dimension by the index of kurtosis and then selecting the best solutions among the various dimensions. The selection scheme and diagnosis performance were verified by the analysis of a group of bearing fault signals added with wheel-track interference. Some characteristics can be found in PSO-MF. Firstly, the optimization scheme is capable of selecting the best solution (or one of the best solutions) among the collected operators. Secondly, by applying kurtosis as the fitness function, the optimized solution of MF reduces the interference of shaft rotation or wheel-track excitement. Thirdly, the PSO-MF has advanced performance on fault diagnosis under the cases with heavy colored noise. Although the performance of PSO-MF on bearing diagnosis of the railway vehicle is excellent, there is still a lot of room for improvement. Only the SE shapes of flat and triangle are considered in the proposed method, and more shape variants can be considered in the future work. The computation of PSO-MF is time consuming; the improvement of the calculation speed of PSO will largely enhance the efficiency

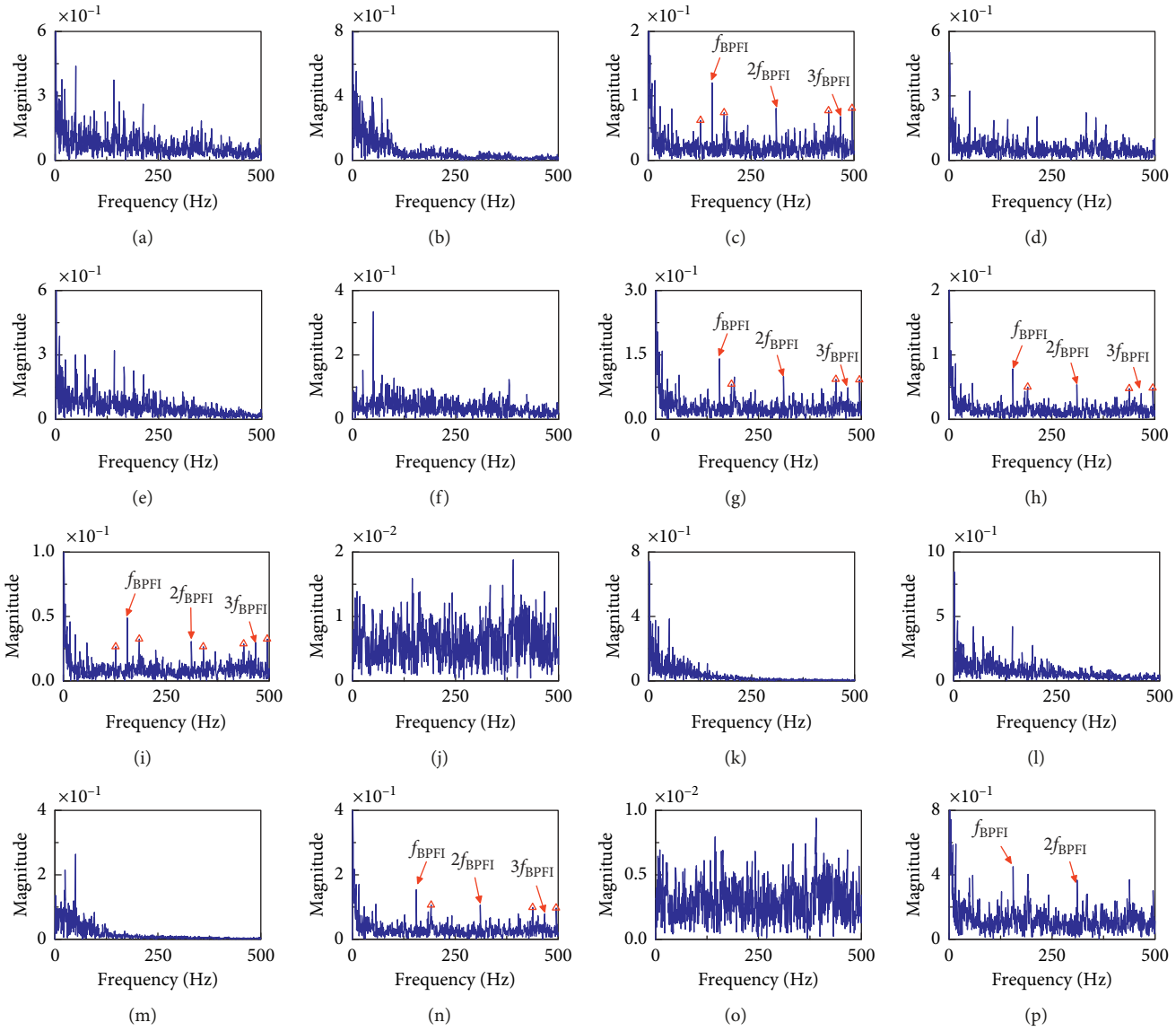

Figure 13: The spectra of collected operations of the inner-race fault signal. (a) Dilation. (b) Erosion. (c) MG. (d) Close. (e) Open. (f) $A_{C\&O}$. (g) DIF. (h) BTH. (i) WTH. (j) $C_{WTH\&PBTH}$. (k) Close-open. (l) Open-close. (m) CMF. (n) $G_{CO\&OC}$. (o) CMFH. (p) MGPO.

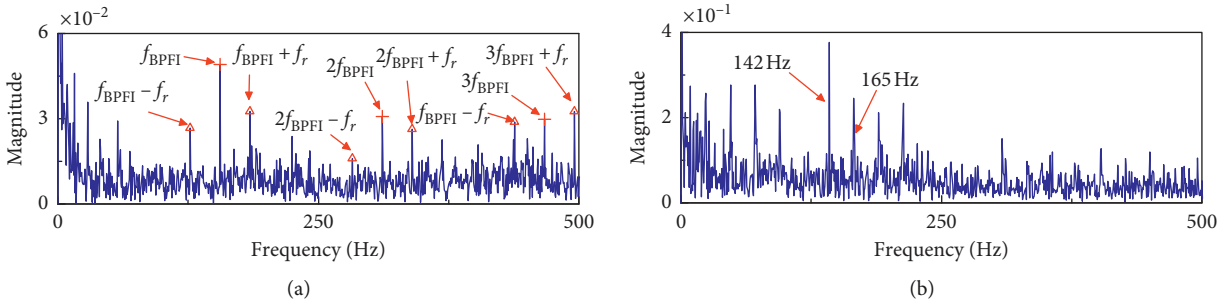

Figure 14: Continued.

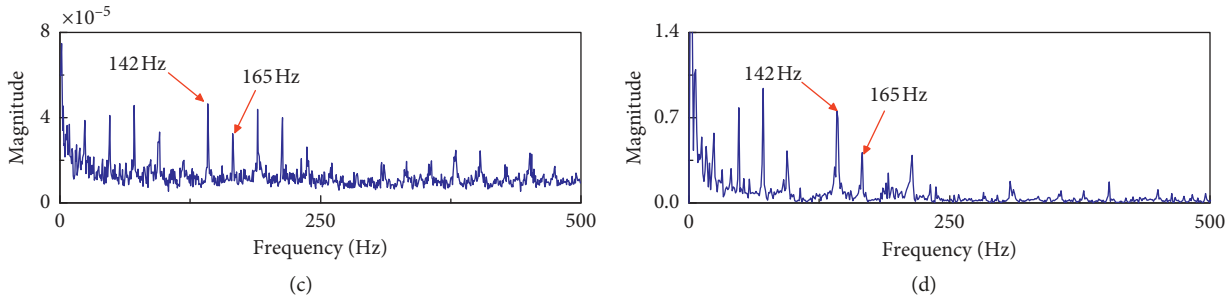

FIGURE 14: The spectra of comparison methods of the inner-race fault signal: (a) PSO-MF, (b) envelope spectrum, (c) enhanced envelope spectrum, and (d) autocorrelation spectrum.

of PSO-MF. With the continuous collection of operators, it will be interesting to compare with as many operators as possible when analyzing the bearing fault signal.

Data Availability

Two data sets are used in this paper: one from SWJTU is conducted with CRRC which is confidential; another data set is from the CWRU which is open, and the website for downloading the data is given in the references.

Conflicts of Interest

The authors declare that they have no conflicts of interest.

Acknowledgments

This work was sponsored by the Ministry of Science and Technology of the People's Republic of China under the following funding program: the China National Key Research and Development Plan for Advanced Rail Transit (grant number 2017YFB1201004).

References

[1] C. Huang, J. Lin, J. Ding, and Y. Huang, "A novel wheelset bearing fault diagnosis method integrated CEEMDAN, periodic segment matrix, and SVD," *Shock and Vibration*, vol. 2018, Article ID 1382726, 18 pages, 2018.

[2] Y. Huang, J. Lin, Z. Liu, and W. Wu, "A modified scale-space guiding variational mode decomposition for high-speed railway bearing fault diagnosis," *Journal of Sound and Vibration*, vol. 444, pp. 216–234, 2019.

[3] J. Ding, "Fault detection of a wheelset bearing in a high-speed train using the shock-response convolutional sparse-coding technique," *Measurement*, vol. 117, pp. 108–124, 2018.

[4] L. Xu and W. Zhai, "A novel model for determining the amplitude-wavelength limits of track irregularities accompanied by a reliability assessment in railway vehicle-track dynamics," *Mechanical Systems and Signal Processing*, vol. 86, pp. 260–277, 2017.

[5] L. Xu, W. Zhai, and J. Gao, "Global sensitivity analysis for vehicle–track interactions: special attention on track irregularities," *Journal of Computational and Nonlinear Dynamics*, vol. 13, no. 3, Article ID 031007, 2018.

[6] H. Zhao, M. Sun, W. Deng, and X. Yang, "A new feature extraction method based on EEMD and multi-scale fuzzy entropy for motor bearing," *Entropy*, vol. 19, no. 1, 2017.

[7] Z. Liu, J. Ding, J. Lin, and Y. Huang, "A rolling bearing fault diagnosis-optimized scale-space representation for the empirical wavelet transform," *Shock and Vibration*, vol. 2018, Article ID 2749689, 22 pages, 2018.

[8] J. Antoni, "Fast computation of the kurtogram for the detection of transient faults," *Mechanical Systems and Signal Processing*, vol. 21, no. 1, pp. 108–124, 2007.

[9] S. Chen, X. Dong, Z. Peng, W. Zhang, and G. Meng, "Nonlinear chirp mode decomposition: a variational method," *IEEE Transactions on Signal Processing*, vol. 65, no. 22, pp. 6024–6037, 2017.

[10] W. Du, Z. Wang, X. Gong, L. Wang, and G. Luo, "Optimum IMFs selection based envelope analysis of bearing fault diagnosis in plunger pump," *Shock and Vibration*, vol. 2016, Article ID 1248626, 8 pages, 2016.

[11] L. Li, Y. Cui, R. Chen, and X. Liu, "Optimal SES selection based on SVD and its application to incipient bearing fault diagnosis," *Shock and Vibration*, vol. 2018, Article ID 8067416, 13 pages, 2018.

[12] J. Antoni, G. Xin, and N. Hamzaoui, "Fast computation of the spectral correlation," *Mechanical Systems and Signal Processing*, vol. 92, pp. 248–277, 2017.

[13] Z. Feng and F. Chu, "Cyclostationary analysis for gearbox and bearing fault diagnosis," *Shock and Vibration*, vol. 2015, Article ID 542472, 12 pages, 2015.

[14] P. Maragos and R. Schafer, "Morphological filters—Part I: their set-theoretic analysis and relations to linear shift-invariant filters," *IEEE Transactions on Acoustics, Speech, and Signal Processing*, vol. 35, no. 8, pp. 1153–1169, 1987.

[15] N. G. Nlkolaou and I. A. Antoniadis, "Application of morphological operators as envelope extractors for impulsive-type periodic signals," *Mechanical Systems and Signal Processing*, vol. 17, no. 6, pp. 1147–1162, 2003.

[16] F. Meyer and P. Maragos, "Nonlinear scale-space representation with morphological levelings," *Journal of Visual Communication and Image Representation*, vol. 11, no. 2, pp. 245–265, 2000.

[17] C. Li and M. Liang, "Continuous-scale mathematical morphology-based optimal scale band demodulation of impulsive feature for bearing defect diagnosis," *Journal of Sound and Vibration*, vol. 331, no. 26, pp. 5864–5879, 2012.

[18] Y. Li, X. Liang, and M. J. Zuo, "Diagonal slice spectrum assisted optimal scale morphological filter for rolling element bearing fault diagnosis," *Mechanical Systems and Signal Processing*, vol. 85, pp. 146–161, 2017.

[19] L. Meng, J. Xiang, Y. Zhong, and W. Song, "Fault diagnosis of rolling bearing based on second generation wavelet denoising and morphological filter," *Journal of Mechanical Science and Technology*, vol. 29, no. 8, pp. 3121–3129, 2015.

[20] L. Meng, J. Xiang, Y. Wang, Y. Jiang, and H. Gao, "A hybrid fault diagnosis method using morphological filter-translation invariant wavelet and improved ensemble empirical mode decomposition," *Mechanical Systems and Signal Processing*, vol. 50-51, pp. 101–115, 2015.

[21] H. Zhao, J. Zheng, J. Xu, and W. Deng, "Fault diagnosis method based on principal component analysis and broad learning system," *IEEE Access*, vol. 7, pp. 99263–99272, 2019.

[22] W. Deng, J. Xu, and H. Zhao, "An improved ant colony optimization algorithm based on hybrid strategies for scheduling problem," *IEEE Access*, vol. 7, pp. 20281–20292, 2019.

[23] W. Deng, H. Zhao, L. Zou, G. Li, X. Yang, and D. Wu, "A novel collaborative optimization algorithm in solving complex optimization problems," *Soft Computing*, vol. 21, no. 15, pp. 4387–4398, 2017.

[24] W. Deng, H. Zhao, X. Yang, J. Xiong, M. Sun, and B. Li, "Study on an improved adaptive PSO algorithm for solving multi-objective gate assignment," *Applied Soft Computing*, vol. 59, pp. 288–302, 2017.

[25] Y. Li, M. J. Zuo, Y. Chen, and K. Feng, "An enhanced morphology gradient product filter for bearing fault detection," *Mechanical Systems and Signal Processing*, vol. 109, pp. 166–184, 2018.

[26] J. Wang, G. Xu, Q. Zhang, and L. Liang, "Application of improved morphological filter to the extraction of impulsive attenuation signals," *Mechanical Systems and Signal Processing*, vol. 23, no. 1, pp. 236–245, 2009.

[27] A. I. N. Press, "The spectral kurtosis : application to the vibratory surveillance and diagnostics of rotating machines," *Mechanical Systems and Signal Processing*, vol. 20, no. 2, pp. 308–331, 2006.

[28] W. A. Smith, Z. Fan, Z. Peng, H. Li, and R. B. Randall, "Optimised Spectral Kurtosis for bearing diagnostics under electromagnetic interference," *Mechanical Systems and Signal Processing*, vol. 75, pp. 371–394, 2016.

[29] Y. Cheng, N. Zhou, W. Zhang, and Z. Wang, "Application of an improved minimum entropy deconvolution method for railway rolling element bearing fault diagnosis," *Journal of Sound and Vibration*, vol. 425, pp. 53–69, 2018.

[30] Case Western Reserve University Bearing Data Center Website, http://csegroups.case.edu/bearingdatacenter/home.

[31] W. A. Smith and R. B. Randall, "Rolling element bearing diagnostics using the Case Western Reserve University data: a benchmark study," *Mechanical Systems and Signal Processing*, vol. 64-65, pp. 100–131, 2015.

[32] P. D. McFadden and J. D. Smith, "Model for the vibration produced by a single point defect in a rolling element bearing," *Journal of Sound and Vibration*, vol. 96, no. 1, pp. 69–82, 1984.